Computational Sciences and Engineering 4(1) (2024) 101-124

University of Guilan

Computational Sciences and Engineering

journal homepage: https://cse.guilan.ac.ir/

Robust Gustafson-Kessel (RGK) Clustering for Segmentation of Brain Tissues Based on MRI images

Ali Fahmi Jafargholkhanloo [a,*], Mousa Shamsi [b], Mahdi Bashiri Bawil [b]

[a] Department of Engineering Sciences, Faculty of Advanced Technologies, University of Mohaghegh Ardabili, Namin, Iran
[b] Faculty of Biomedical Engineering, Sahand University of Technology, Tabriz, Iran

ARTICLE INFO

Article history:
Received 22 October 2024
Received in revised form 30 January 2025
Accepted 05 February 2025
Available online 05 February 2025

Keywords:
Brain MRI Segmentation
Fuzzy c-means
Gustafson-Kessel
Image Segmentation
Wiener Filter

ABSTRACT

The fuzzy c-means (FCM) algorithm is widely used for image segmentation based on clustering. However, it is sensitive to noise, and its convergence is affected by the data distribution. FCM relies on the Euclidean distance metric, which fails to account for variations in the distances within similar and compact clusters. Moreover, the distance metric is not locally adaptive to the shape of clusters. This paper introduces a robust Gustafson-Kessel (RGK) clustering algorithm to address these limitations for brain tissue segmentation using MRI images. To achieve accurate segmentation under varying noise levels and intensity non-uniformity (INU), a Wiener filter integrated with wavelet transform (WFWT) is employed as a preprocessing step to enhance image quality while preserving object edges. The Mahalanobis distance is used for clustering to better adapt to the shape of the clusters. Additionally, the RGK algorithm incorporates membership matrix filtering to exploit the local spatial constraint. The proposed RGK algorithm was evaluated using two datasets: the BrainWeb simulated dataset and MRI scans from 10 healthy individuals at the Golghasht Medical Imaging Center in Tabriz (GMICT), Iran. In RGK, it is not necessary to compute the distance between pixels within local spatial neighbors and clusters. Experimental results demonstrate that the RGK algorithm outperforms traditional FCM-based methods in the segmentation of brain tissues.

1. Introduction

Medical image analysis is an essential step in clinical assessment that depends on the accuracy of the segmentation process. Medical image segmentation (MIS) is a necessary stage in smart medicine due to significant improvements in assessment performance. The MIS process separates the desired

* Corresponding author.
E-mail addresses: a_fahmi@uma.ac.ir (A. Fahmi Jafargholkhanloo)

https://doi.org/10.22124/cse.2025.28776.1088

regions for behavioral analysis and morphological changes of different regions to detect diseases [1-3]. This process in magnetic resonance imaging (MRI) depends on many factors, such as intensity non-uniformity (INU), noise, proximity of tissues to each other, and the intrinsic properties of brain tissues. INU often causes incorrect segmentation of brain tissues due to the overlap in the intensity ranges of different tissues [1, 4]. MRI is a popular imaging modality suitable for examining tissue-level details. There are three main tissues in the human brain: cerebrospinal fluid (CSF), gray matter (GM), and white matter (WM), which play a vital role in quantitative brain analysis for diagnostic purposes. Additionally, the quality of MRI images depends on the gray levels of these tissues. Several brain disorders, such as multiple sclerosis (MS), schizophrenia, and Alzheimer's disease, can be recognized in these regions [5-8]. Distinguishing between different brain tissues is a major challenge for many radiologists. Manual segmentation is time-consuming and can produce inconsistent findings due to intra-observer and inter-observer variability. Therefore, radiologists need an accurate automated approach for segmenting multiple brain regions. Different approaches, such as thresholding-based methods, clustering-based methods, contour-based methods, and deep learning-based methods, have been developed for medical image segmentation [9, 10]. Threshold-based methods [11, 12] assign pixels to suitable categories by calculating single or multiple gray thresholds for the image. These approaches often lack efficiency in the presence of artifacts, noise, and fluctuations in gray-scale values [13]. Contour-based methods [14, 15] segment the image by constructing an energy function. These methods require an initial contour and tuning of parameters. Moreover, they cannot effectively track topological changes of objects and perform poorly when INU is present in the image [16]. Deep learning-based methods face drawbacks such as slow training speed, dependence on data volume, and complex structures [10]. One of the most popular image segmentation techniques is clustering, which partitions a set into clusters so that members of the same cluster are similar, while members of different clusters are dissimilar. To address the aforementioned problems, this study focuses on these methods.INU in MRI can result from many factors, including B1 and B0 field inhomogeneities and patient-specific interactions. Therefore, bias correction is often an essential step to remove INU before performing quantitative analysis of MRI images. Li et al. [4] presented a new energy minimization method called multiplicative intrinsic component optimization (MICO) for MRI bias field estimation and tissue segmentation. Adhikari et al. [17] proposed a conditional spatial fuzzy c-means (CSFCM) clustering algorithm to improve the performance of conventional FCM clustering for the segmentation of MRI tissues. Elazab et al. [18] introduced an adaptively regularized kernel-based FCM (ARKFCM) for segmenting multiple tissues based on MRI images. Bakhshali [19] presented an improved and robust FCM method based on information theory to estimate and correct INU while minimizing noise effects. Moeskops et al. [20] developed a convolutional neural network (CNN) for automatic segmentation of MRI brain images. Ghosh et al. [21] introduced a spatial modified FCM algorithm to address noise and INU in MRI images. Conventional FCM is sensitive to initialization; hence, this method applied a chaotic firefly algorithm (CFA) to mitigate this issue. Hassan et al. [5] proposed a robust spatial fuzzy Gaussian mixture model (GMM) for segmenting MRI and ultrasound imaging modalities. Kouhi et al. [1] introduced a robust FCM algorithm combining spatial constraints and local information from the membership matrix for brain MRI segmentation. Threshold-based methods are popular for image segmentation that utilize histogram images. Bandyopadhyay et al. [3] presented an altruistic Harris hawk optimization (AHHO) for the segmentation of brain MRI images. One drawback of conventional FCM is its tendency to frequently get trapped at local minima. To overcome this challenge, Verma et al. [22] proposed a population-based hybrid FCM with particle swarm optimization (FCMPSO) for brain image segmentation. Tongbram et al. [23] presented a novel approach using FCM and the whale optimization algorithm (FCMWOA) to address this issue. Natarajan et al. [9] proposed a minimally parametrized segmentation approach with dual metaheuristic optimization algorithms (including artificial bee colony (ABC) and JAYA algorithm) in conjunction with FCM for the detection of anomalies in MRI brain images. Conventional FCM performs poorly in the presence of imaging artifacts due to its disregard for spatial information. To address this problem, Chighoub and Saouli [24] presented a fully integrated approach that incorporates spatial information for brain MRI image segmentation. Kumar et al. [25] introduced kernel picture FCM with spatial neighborhood information for MRI image segmentation in the presence of vague boundary structures, noise, and nonlinearity. Identifying boundary information in brain images is difficult because of low contrast. Khaled et al. [26] developed a learning method to detect boundary information for brain image segmentation. Khatri et al. [27] introduced picture fuzzy set-based clustering to address noise, vagueness, and non-linear structures in an image, termed kernel FCM for picture fuzzy set, using the Kullback-Leibler divergence measure (KFPKL).MRI image segmentation becomes increasingly challenging in the presence of artifacts such as noise, partial volume effects, and bias field effects. Kumar et al. [28] proposed the bias-corrected intuitionistic FCM with spatial neighborhood information (BCIFCMSNI) to tackle these issues. Emam et al. [2] presented a modified reptile search algorithm (MRSA) for global optimization, selecting optimal thresholding values for multilevel brain image segmentation. The segmentation of MRI images is influenced by sudden changes in intensity between the boundaries of brain tissues. Singh et al. [6] introduced an intuitionistic FCM and local information-based discrete cosine transform (DCT) filtering for rapid brain MRI segmentation. Kollem et al. [29] presented an optimized multi-kernel FCM method for brain tumor MRI image segmentation. MRI image segmentation is a challenging problem due to spatially distributed noise and uncertainty at the boundaries of soft tissues. To address this challenge, Solanki and Kumar [30] proposed probabilistic intuitionistic FCM with spatial constraints (PIFCMSC). Alagarsamy et al. [31] introduced ABC combined with an interval type-II fuzzy logic system algorithm for brain tumor segmentation. Kalti and Touil [32] proposed a robust contextual FCM to address the sensitivity of the FCM algorithm to noise when clustering image pixels. Mohammadi et al. [33] presented a case series using marker-controlled watershed segmentation and FCM for meningioma segmentation from contrast-enhanced T1-weighted MRI images. Singh et al. [8] introduced a novel method based on incorporating local spatial and gray level information for segmenting MRI images under INU and noisy conditions. Houssein et al. [10] proposed a threshold-based method using an oppositional snake optimization algorithm (OSOA) for segmentation of computed tomography (CT) liver images. Shekari and Rostamian [34] presented a contour-based method and FCM for brain tumor segmentation from MRI images. Tian and Wang [35] developed a level set model (contour-based approach) for segmentation of intervertebral disc MRI images. Conventional FCM is sensitive to noise and initialization. To address these problems, optimized FCM approaches such as FCMPSO and FCMWOA have been presented, but these methods often lack appropriate performance under different INU conditions. Additionally, many population-based optimization algorithms, such as PSO, require parameter tuning to balance exploration and exploitation phases, and these parameters can significantly impact segmentation accuracy. Kernel-based approaches, such as ARKFCM, are usually ineffective for non-spherical data and tend to be computationally intensive. In level set-based methods, such as MICO, the edge-stopping function depends on the image gradient. This reliance causes only objects with edges defined by the gradient to be segmented. The implicit functions in these approaches require frequent reinitialization to maintain the signed distance property [36]. Threshold-based methods, such as AHHO and OSOA, are unsuitable for images with flat and broad valleys. These methods typically neglect spatial information during the segmentation process and are extremely sensitive to noise and INU. Picture fuzzy system approaches, such as KFPKL, often lack sufficient robustness against noise and outliers. Deep learning-based methods require substantial computational resources, graphics processing units (GPUs), and large amounts of memory, making them time-consuming. Furthermore, these methods are dependent on the volume and quality of the data. The dissimilarity index in presented FCM-based methods, such as FCM, KFPKL, and BCIFCMSNI, is not always a representative point for compact clusters. Using the Euclidean distance in these approaches disregards the variation in distance among data points in similar clusters. Moreover, the performance of FCM-based methods is generally satisfactory only when the clusters in the data are roughly the same size and shape. To overcome these problems, we propose a robust Gustafson-Kessel (RGK) algorithm for brain tissue segmentation based on MRI images. This study presents a novel RGK clustering algorithm that enhances segmentation accuracy across various noise and INU conditions. Our key contributions are as follows:

1. A significant challenge in MRI analysis is that the intensities are acquired in arbitrary units, resulting in variations between scanning parameters and studies that may exceed the actual biological differences in the images. To address this issue, we propose using a brain extraction method to mitigate these inconsistencies. Additionally, to overcome noise and intensity non-uniformity (INU) while preserving image details, we introduce a preprocessing step using a Wiener filter combined with a wavelet transform (WFWT).
2. The proposed RGK algorithm introduces a novel image segmentation method for MRI by considering clusters with elliptical shapes. Unlike other FCM-based algorithms, which assume hyper-spherical cluster shapes, the RGK algorithm accommodates the elliptical geometry, enabling more accurate segmentation. This approach allows the RGK algorithm to better preserve image details, even in the presence of high noise levels and varying intensity non-uniformity (INU) conditions.
3. The proposed method does not require parameter tuning, simplifying its application.
4. The performance of the proposed RGK algorithm was validated using 41 brain MRI images from the BrainWeb dataset under various noise and INU conditions. Additionally, it was tested on 10 healthy individuals who underwent imaging at the Golghasht Medical Imaging Center in Tabriz (GMICT), Iran. The RGK algorithm's performance was further compared to several FCM-based approaches, using average Dice, Jaccard, and contour matching criteria for evaluation.

The remainder of this article is structured as follows: Section 2 reviews FCM and GK algorithms. Section 3 presents the proposed RGK algorithm. Section 4 details the datasets used and the experimental results. Finally, Section 5 concludes the study and suggests directions for future research.

2. FCM and GK Clustering Algorithms

Soft and hard clustering methods are two approaches for clustering process. In soft clustering, every pixel can be allocated to all clusters with different membership values. FCM is the most popular soft clustering method. In K-Means clustering, only one cluster is allocated to each point, but in

FCM one cluster can be allocated to two or more clusters [37]. The FCM algorithm is presented by Bezdek [38] which improves the performance of K-means based on membership matrix u_{ij}. For an image *I(x,y)* with grayscale values x_i $(i = 1, 2, \dots, N)$ and cluster centers $V = \{v_1, v_2, \dots, v_C\}$ there is a membership value u_{ij} for each pixel *i* in the *j*th clusters *(j=1, 2,..., c)*. The cost function in FCM is defined as follows:

$$J_{FCM} = \sum_{i=1}^{N} \sum_{j=1}^{c} u_{ij}{}^{q} \left(x_i - v_j\right)^2 \quad \textbf{(1)}$$

with the following constraint:

$$\sum_{j=1}^{c} u_{ij} = 1 \ \forall i \quad \textbf{(2)}$$

where v_j and q *(q>1)* are cluster center and fuzzy exponent, respectively.

In FCM, the membership function and cluster centers are iteratively updated as follows:

$$u_{ij} = \frac{1}{\sum_{j=1}^{c} \left(\frac{\|x_i - v_k\|^2}{\|x_i - v_j\|^2} \right)^{\frac{2}{q-1}}} \quad \textbf{(3)}$$

$$v_j = \frac{\sum_{i=1}^{N} (u_{ij}{}^{q} x_i)}{\sum_{i=1}^{N} (u_{ij}{}^{q})} \quad \textbf{(4)}$$

The algorithmic steps involved for FCM is summarized in Algorithm 1.

Algorithm 1: FCM algorithm steps

Input: MRI image, number of cluster centers, fuzzy exponent q, and stop criterion η
***Step 1*:** Initialization membership matrix $U^{(\tau)}$
Step 2: Update cluster centers $v^{(\tau+1)}$ using Eq. (4).
Step 3: Update membership matrix $U^{(\tau+1)}$ using Eq. (3).
Step 4: if max$\left\|U^{(\tau+1)} - U^{(\tau)}\right\| \leq \eta$, then stop, otherwise set $\tau = \tau + 1$ and go
Step 2
Output: cluster centers and membership matrix.

In FCM, the clusters are assumed to be spherical. Therefore, the performance of FCM is adequate when the clusters in the data are roughly the same size and shape. In contrast, the GK algorithm is suitable for detecting ellipsoidal cloud clusters with varying sizes and orientations to different degrees [39, 40]. The main characteristic of GK is its local adaptation of the distance index to the cluster shape by estimating the covariance matrix [41]. Gustafson and Kessel [42] suggested an extension of FCM to detect different geometrical shapes by using the Mahalanobis distance instead of the Euclidean distance in FCM. The cost function in GK is defined as follows:

$$J_{GK} = \sum_{i=1}^{N} \sum_{j=1}^{c} u_{ij}{}^{q} . \left(x_i - v_j\right)^T . A_j . \left(x_i - v_j\right) \quad \textbf{(5)}$$

where the norm matrix A_j is a positive definite symmetric matrix. Utilizing the Lagrange multiplier technique, ***Eq. (4)*** can be converted to an unconstrained optimization problem that minimizes the following cost function:

$$J_{GK} = \sum_{i=1}^{N} \sum_{j=1}^{c} u_{ij}{}^{q} . \left(x_i - v_j\right)^T . A_j . \left(x_i - v_j\right) - \sum_{i=1}^{N} \lambda_i \left(\sum_{j=1}^{c} u_{ij} - 1\right) + \sum_{j=1}^{c} \beta_j . \left(det\left(A_j\right) - \rho_j\right) \quad \textbf{(6)}$$

where β_j a set of Lagrange multipliers. Also, ρ_j is a cluster volume which is usually considered to 1 for each cluster.

The membership function, cluster centers, and covariance matrix are updated as follows:

$$u_{ij} = \left(\frac{(x_i - v_r)^T . A_r . (x_i - v_r)}{\sum_{j=1}^{c} (x_i - v_j)^T . A_j . (x_i - v_j)}\right)^{1/q-1} \quad \textbf{(7)}$$

$$v_j = \frac{\sum_{i=1}^{k} u_{ij}{}^q . x_i}{\sum_{i=1}^{k} u_{ij}{}^q} \quad \textbf{(8)}$$

$$F_i = \frac{\sum_{i=1}^{N} u_{ij}{}^q . (x_i - v_j)^T . (x_i - v_j)}{\sum_{i=1}^{N} u_{ij}{}^q} \quad \textbf{(9)}$$

$$A_j = \lambda_i . \left(det(F_i)\right)^{\frac{1}{n}} . F_i{}^{-1} \quad \textbf{(10)}$$

The algorithmic steps involved for GK is summarized in Algorithm 2.

Algorithm 2: GK algorithm steps

Input: MRI image, number of cluster centers, fuzzy exponent q, and stop criterion η
Step 1: Initialization membership matrix $U^{(\tau)}$
Step 2: Update cluster centers $v^{(\tau+1)}$ using Eq. (8).
Step 3: Update covariance matrix $F^{(\tau+1)}$ using Eq. (9).
Step 4: Update norm matrix $A^{(\tau+1)}$ using Eq. (10).
Step 5: Update membership matrix $U^{(\tau+1)}$ using Eq. (7).
Step 6: if max$\left\| U^{(\tau+1)} - U^{(\tau)} \right\| \leq \eta$, then stop, otherwise set $\tau = \tau + 1$ and go
Step 2
Output: cluster centers, covariance matrix, and membership matrix.

3. Proposed Algorithm

The dissimilarity index in the presented FCM-based methods is not usually representative of compact clusters. Using the Euclidean distance in these approaches disregards the distance variation of data points within similar clusters. Therefore, there are challenges in image segmentation. To address these issues, this study proposes a robust GK (RGK) algorithm. As shown in ***Figure 1***, a Wiener filter, combined with wavelet transform, is first applied to address the noise and INU problems. In the next step, motivated by the ideas of EnFCM [43] and FRFCM [44], we obtain the gray-level histogram of a reconstructed image. Then, the Mahalanobis distance is employed instead of the Euclidean distance. In the following step, the cluster centers, membership matrix, and positive definite symmetric matrix are updated via an iterative operation. Finally, a median filter is used to modify the membership partition matrix. By applying this method, we can achieve good segmentation results in grayscale MRI images, requiring less elapsed time.

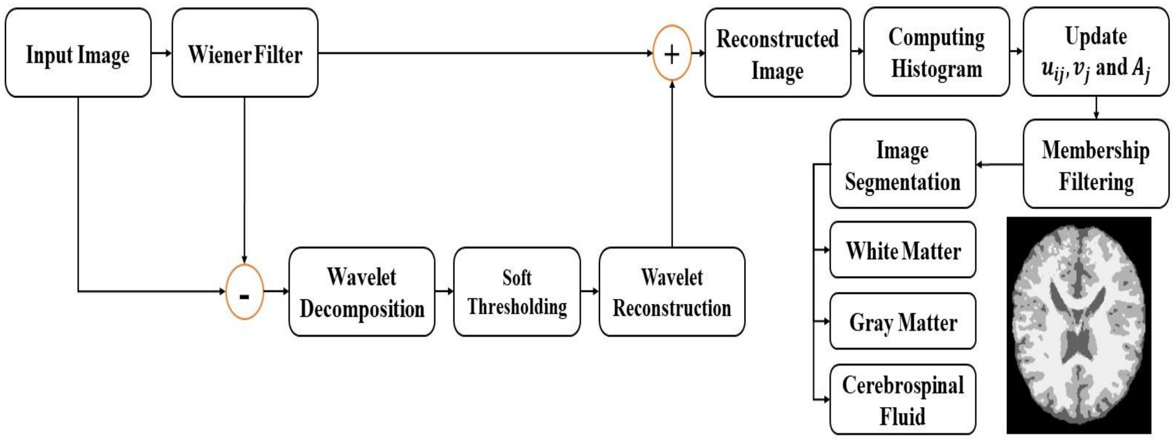

***Figure* 1.** Block-diagram of the proposed RGK algorithm for segmentation of brain tissues based on MRI images.

3.1. Wiener Filter by Cooperating Wavelet Transform

The existence of noise and INU affects the performance of the clustering process. On the other hand, the distribution properties of the data are also impacted by noise and INU. This situation leads to three problems: (1) the segmentation performance is inadequate for noisy images, (2) the number of iterations for the FCM and GK algorithms is larger for images corrupted by noise than for images that are uncorrupted, and (3) obtaining the image histogram for fast image segmentation is difficult under noisy and INU conditions [44]. To address these problems, this study introduces the WFWT approach as a preprocessing step for the GK algorithm before applying the clustering process to optimize the distribution characteristics of the data. We used three common methods, including mean, median, and Wiener filters, for image denoising. As shown in ***Figure 2***, the Wiener filter demonstrates good performance for MRI image denoising under 9% noise and 40% INU conditions. The Wiener filter is applied to estimate the pixel value by using the local pixel average and the variance of the neighboring pixels [45]. In this process, the local mean value μ and the local variance value σ^2 for the pixel at the location (k, r) of the noisy image $\mathcal{N}$ are computed as follows:

$$\mu(k,r) = \frac{1}{(2M+1)(2N+1)}\sum_{m=-M}^{M}\sum_{n=-N}^{N}\text{Ɲ}(k+m,r+n) \quad \textbf{(11)}$$

$$\sigma^2(k,r) = \frac{1}{(2M+1)(2N+1)}\sum_{m=-M}^{M}\sum_{n=-N}^{N}\text{Ɲ}^2(k+m,r+n) - \mu^2(k+m,r+n) \quad \textbf{(12)}$$

where the dimensions of filter kernel are $(2M+1)\times(2N+1)$.

Also, filtered image matrix $\text{Ɲ}(k,r)$ at the location (k, r) is obtained as follows:

$$\text{Ɲ}(k,r) = \mu(k,r) + \frac{\sigma^2(k,r)}{\sigma^2(k,r)+\sigma_{\text{Ɲ}}{}^2}\left(\text{Ɲ}(k,r) - \mu(k,r)\right) \quad \textbf{(13)}$$

where $\sigma_{\text{Ɲ}}{}^2$ is the variance of noisy image. If this criterion is not given, the average of all the local estimates of the variances is used as the variance of noisy image.

Generally, motivated by the presented idea in [46], difference between the original image and denoised image ($\mathcal{F}$) must be close zero. As shown in ***Figure 3(c)***, $\mathcal{F}$ is included the information that can be defined as follows:

$$\text{Ƒ} = \text{Ş} + \text{Ŋ} \quad \textbf{(14)}$$

where Ş and Ŋ remained information from original and noisy signals, respectively.

Now, the challenge is to estimate the $\mathcal{Ş}$ and add it to input image. For this purpose, wavelet transform is applied. This process, can be defined as follows:

$$\mathcal{W}_{\mathrm{F}} = \mathcal{W}_{\mathrm{Ş}} + \mathcal{W}_{\mathrm{N}} \tag{15}$$

where $\mathcal{W}_{\mathrm{Ş}}$ and $\mathcal{W}_{\mathrm{N}}$ are remained signal and noisy wavelet coefficients, respectively.

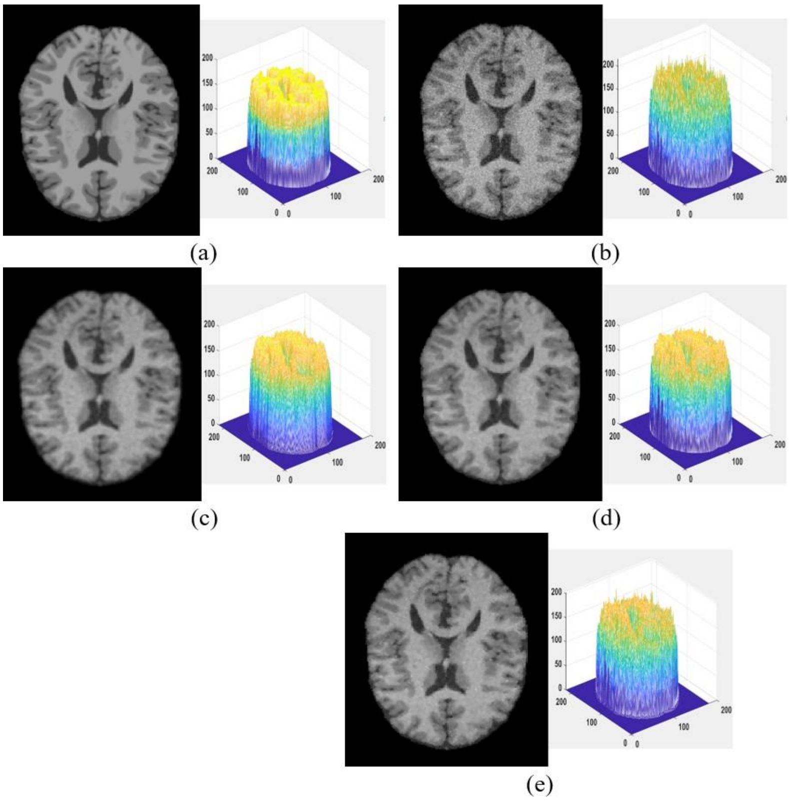

Figure 2. Comparison of noise removal using different filters. (a): Original image. (b): Image corrupted by 9% noise and 40% INU. (c): Filtered image using mean filtering. (d): Filtered image using median filtering. (e): Filtered image using Wiener filtering.

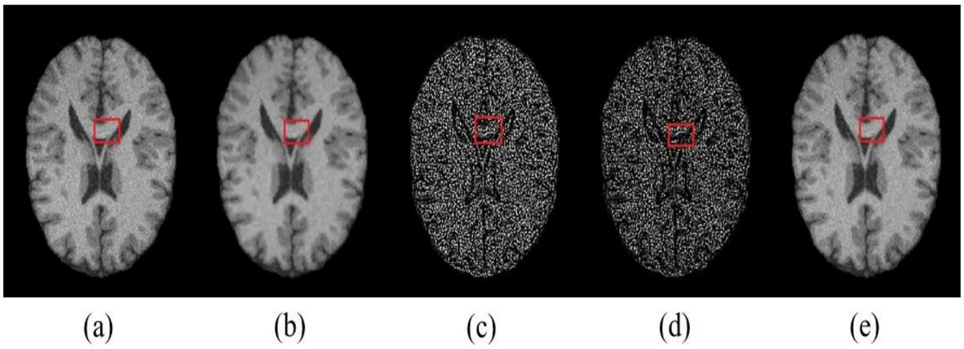

85	104	65	119	119
52	64	95	137	114
45	78	122	140	99
55	84	131	123	54
72	133	135	115	76

87	104	73	116	117
59	68	97	129	112
57	79	119	133	99
58	86	126	120	61
73	129	127	113	79

-2	0	-8	3	2
-7	-4	-2	8	2
-12	-1	3	7	0
-3	-2	5	3	-7
-1	4	8	2	-3

-1	-1	-5.1	2.8	0.7
-2.9	-2.9	-2.1	5.7	0.7
-6.8	-1	2.9	3.2	0.5
-3	-2	3.2	2.9	-6.5
0	0.8	4.4	0.1	-1.1

84	103	59.9	121.8	119.7
49.1	61.1	92.9	142.7	114.7
38.2	77	124.9	143.2	99.5
52	82	134.2	125.9	47.5
72	133.8	139.4	115.1	74.9

Figure 3. The steps of WFWT approach. (a): Noisy image. (b): Denoised image by applying Wiener filter. (c): Difference between the (*a*) and (*b*) steps ($\mathcal{F}$). (d): Output of decomposition process with wavelet transform. (e): Fina reconstructed image by adding (*d*) step to (*a*) step.

As show in ***Figure 3(d-e)***, by applying wavelet transform on $\mathcal{F}$ and extracting the $\mathcal{Ş}$, we could to remove more noise. This process causes that the presented RGK algorithm to be more robust to noise and INU conditions. In this study, Haar wavelet is used for decomposition process and soft-thresholding is applied to threshold these wavelet coefficients. Also, decomposition process is performed to five levels.

3.2. Robust Gustafson-Kessel

Based on the obtained gray level histogram of the reconstructed image ξ_i by WFWT (a weighted sum image based on original image and its local neighbor average), we proposed the cost function of RGK for image segmentation as follows:

$$J_{RGK} = \sum_{i=1}^{k} \sum_{j=1}^{c} \gamma_i . u_{ij}{}^{q} . \left(\xi_i - v_j\right)^T . A_j . \left(\xi_i - v_j\right) \quad (16)$$

where γ_i is the number of pixels with gray value equal to i $(i = 1, 2, \ldots, k)$. Generally, we have:

$$\sum_{i=1}^{k} \gamma_i = N \quad (17)$$

Utilizing the Lagrange multiplier technique, the aforementioned equation can be converted to an unconstrained optimization problem that minimizes the following cost function:

$$J_{IGK} = \sum_{i=1}^{k} \sum_{j=1}^{c} \gamma_i . u_{ij}{}^{q} . \left(\xi_i - v_j\right)^T . A_j . \left(\xi_i - v_j\right) - \sum_{i=1}^{k} \lambda_i \left(\sum_{j=1}^{c} u_{ij} - 1\right) + \sum_{j=1}^{c} \beta_j . \left(det\left(A_j\right) - \rho_j\right) \quad (18)$$

where λ is a Lagrange multiplier.

The derivative of J_{RGK} relative to u_{ij} and its equality to zero lead to:

$$\frac{\partial J_{IGK}}{\partial u_{ij}} = q . \gamma_i . u_{ij}{}^{q-1} . \left(\xi_i - v_j\right)^T . A_j . \left(\xi_i - v_j\right) - \lambda_i = 0 \quad (19)$$

Eq. (19) is used to update the membership matrix:

$$u_{ij} = \left(\frac{\left(\xi_i - v_r\right)^T . A_r . \left(\xi_i - v_r\right)}{\sum_{j=1}^{c} \left(\xi_i - v_j\right)^T . A_j . \left(\xi_i - v_j\right)}\right)^{1/q-1} \quad (20)$$

To obtain the cluster centers, the partial differential equation of J_{RGK} with respect to v_j is computed and then equaled to zero:

$$\frac{\partial J_{IGK}}{\partial v_j} = -2 \sum_{i=1}^{k} \gamma_i . u_{ij}{}^{q} . \left(\xi_i - v_j\right) . A_j = 0 \quad (21)$$

$$v_j = \frac{\sum_{i=1}^{k} \gamma_i . u_{ij}{}^{q} . \xi_i}{\sum_{i=1}^{k} \gamma_i . u_{ij}{}^{q}} \quad (22)$$

In the final step, the partial differential equation of J_{RGK} with respect to A_j is computed and then equaled to zero:

$$\frac{\partial J_{IGK}}{\partial A_j} = \sum_{i=1}^{k} \gamma_i . u_{ij}{}^{q} . \left(\xi_i - v_j\right)^T . \left(\xi_i - v_j\right) - \sum_{i=1}^{k} \left(\lambda_i . \frac{\partial}{\partial A_j}\left(det\left(A_j\right)\right)\right) = \sum_{i=1}^{k} \gamma_i . u_{ij}{}^{q} . \left(\xi_i - v_j\right)^T . \left(\xi_i - v_j\right) - \sum_{i=1}^{k} \left(\lambda_i . u_{ij}{}^{q} . A_j{}^{-1}\right) = 0 \quad (23)$$

By solving ***Eq. (23)***, the corresponding solutions for A_j is obtained as follows:

$$F_i = \frac{\sum_{i=1}^{k} \gamma_i . u_{ij}{}^{q} . \left(\xi_i - v_j\right)^T . \left(\xi_i - v_j\right)}{\sum_{i=1}^{k} u_{ij}{}^{q}} \quad (24)$$

$$A_j = \lambda_i . \left(det\left(F_i\right)\right)^{\frac{1}{n}} . F_i{}^{-1} \quad (25)$$

Also, a membership function is improved by median filter to speed up the convergence and obtain a better membership matrix as follows:

$$u_{ij}{}^{new} = medfilt\left\{u_{ij}\right\} \quad (26)$$

The algorithmic steps involved for RGK is summarized in Algorithm 3.

Algorithm 3: RGK algorithm steps

Input: MRI image, number of cluster centers, fuzzy exponent q, stop criterion η, and set window size.
Step 1: Compute the new image ξ using WFWT, and then compute the histogram of reconstructed image ξ.
Step 2: Initialization membership matrix $U^{(\tau)}$
Step 3: Update cluster centers $v^{(\tau+1)}$ using ***Eq. (22)***.
Step 4: Update covariance matrix $F^{(\tau+1)}$ using ***Eq. (24)***.
Step 5: Update norm matrix $A^{(\tau+1)}$ using ***Eq. (25)***.
Step 6: Update membership matrix $U^{(\tau+1)}$ using ***Eq. (20)***.
Step 7: if $\max\left\|U^{(\tau+1)} - U^{(\tau)}\right\| \leq \eta$, then stop, otherwise set $\tau = \tau + 1$ and go
Step 3
Step 8: Apply median filter to membership function.
Output: cluster centers, covariance matrix, and membership matrix.

4. Experimental Results

In this section, we present the experimental results and report numerical findings on grayscale MRI images. We also provide segmentation comparisons between the proposed robust GK (RGK) algorithm and other existing algorithms available in the literature, including MICO [4], ARKFCM [18], FCMPSO [22], FCMWOA [23], BCIFCMSNI [28], fast and robust FCM (FRFCM) [44], and residual FCM (RFCM) [47]. The comparisons are conducted both visually and quantitatively. The experiments were performed on an Acer desktop with an Intel Core i7–9750H CPU, operating at a speed of 2.60 GHz, and equipped with 16 GB of RAM.

To evaluate the performance of different algorithms for MRI image segmentation, we used three criteria: the Dice Similarity (*DS*), Jaccard Similarity (*JS*), and Contour Matching Score (*CS*) [48]. The *DS* index measures the degree of overlap between the segmented image and the ground truth (GT). The *JS* index computes the similarity between the two images, while the *CS* index evaluates the contour matching score between the segmented image and the GT. This index ranges from 0 to 1, where a score of 1 indicates that the contours of the objects in the segmented image and the GT match perfectly.

$$DS(A,B) = \frac{2|A \cap B|}{|A|+|B|} \quad \textbf{(27)}$$

$$JS(A,B) = \frac{|A \cap B|}{|A \cup B|} \quad \textbf{(28)}$$

$$CS = \frac{2.P^c.R^c}{P^c+R^c} \quad \textbf{(29)}$$

where P^c and R^c are precision and recall, respectively.

4.1. Data Description

To evaluate the performance of proposed RGK algorithm and other methods, experiments carried out on two brain MRI dataset, namely Brain Web simulated dataset [49] and GMICT dataset, respectively. This dataset consists of many simulated brain MRI images with the different noise level and INU of resolution 1 mm with 181 × 217 × 181 dimensions with the given GT for different brain tissues. In this study, the segmentation process is performed for simulated brain MRI T1-weighted (T1w) and T2-weighted (T2w) brain images having different levels of noise (3% and 9%) and INU (20%, and 40%) on slice 80 to 120. The second data consisted of 10 healthy individuals who underwent imaging using a 1.5-Tesla TOSHIBA Vantage scanner (Canon Medical Systems, Japan) at the Golghasht Medical Imaging Center in Tabriz (GMICT), Iran. The MRI scanning protocols followed standardized procedures, including T1-weighted sequence (repetition time (*TR*) = 540 ms, echo time (*TE*) = 15 ms, flip angle (*FA*) =70◦, field of view (*FOV*) = 230 × 230 mm2, number of slices = 18, acquisition matrix = [0, 256, 176, 0], voxel size = 0.45 × 0.45, slice thickness = 6 mm) , T2-FLAIR sequence (*TR* = 10000 ms, *TE* = 100 ms, , inversion time (*TI*) = 2500 ms, *FA* = 90◦, *FOV* = 230 × 230 mm2, number of slices = 20, acquisition matrix = [0, 256, 192, 0], voxel size = 0.9 × 0.9, slice thickness = 6 mm). A neuroradiologist carefully reviewed all patient scans. The study utilized T1 and T2-FLAIR images with voxel sizes of (0.45, 0.45, 6) and (0.9, 0.9, 6) millimeters, respectively. Ethical approval was obtained from the Tabriz University of Medical Sciences Research Ethics Committee, and written consent was obtained from all participants. In this study, we utilized the 100 T2-FLAIR and T1 images acquired horizontally with the voxel sizes of (0.9, 0.9, 6) and (0.45, 0.45, 6) millimeters, respectively. The Research Ethics Committee of Tabriz University of Medical Sciences granted ethical approval for this study. Additionally, written consent was obtained from all participants. Examples of the GMICT dataset are illustrated in ***Figure 4.*** Morphological operations were utilized for skull stripping.

In recent years, there has been a noticeable rise in the number of neuroimaging studies conducted across multiple sites. However, a significant challenge arises from the fact that MRI intensities are acquired in arbitrary units. This often leads to the realization that the differences in MRI intensities between scanning parameters and studies are larger than the actual biological differences observed in the images. Consequently, normalizing intensity values becomes crucial for accurately analyzing changes in intensities over time and for segmenting different tissues and structures.

The issue of intensity normalization has been extensively addressed in the existing literature, with various methods proposed [50]. These methods range from histogram-based approaches to statistical techniques such as min-max and z-score normalization. For example, [51] developed a method called White Stripe, which applies a z-score transformation to the entire brain using parameters estimated from a latent sub-distribution of normal-appearing white matter (NAWM). This method is particularly suitable for studies involving brain abnormalities, such as MS lesions, as it effectively standardizes the white matter across different subjects. However, it has been observed that residual variability across subjects still persists in gray matter (GM). While common intensity normalization methods successfully correct for global intensity shifts associated with scanner sites, substantial technical variation between scans remains, commonly referred to as the "scan effect" [52]. This technical variation can be attributed to various factors, including scanning parameters, scanner manufacturers, scanner field strength, and more.

To develop a more applicable method, a few reliable references within images could facilitate thorough normalization. In this article, we use the remnants from applying a brain extraction method [53] to obtain reliable values that remain consistent across slices and scans of subjects, even over time. Given that we utilize T1 and T2-FLAIR images, it is well-established that the scalp and skull represent the brightest areas [54, 55]. Specifically, for the given image (I), a brain extraction method is initially applied, resulting in a remnant image (R) obtained by excluding I using the brain mask.

The averages of the first and last deciles of R's intensities are calculated as the minimum and maximum values. Finally, image I is normalized based on these values using the min-max method as follows:

$$x' = \frac{x - x_{min}}{x_{max} - x_{min}} \quad \textbf{(30)}$$

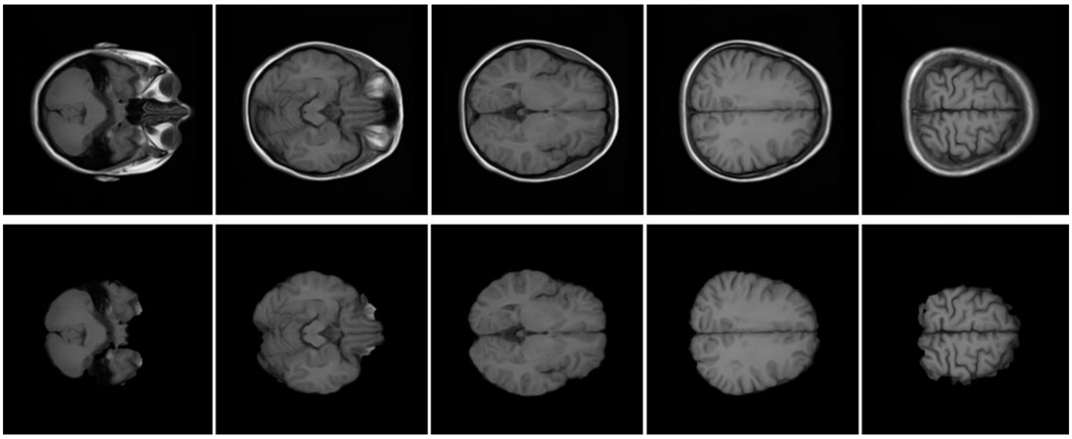

Figure 4. Examples of GMICT dataset. (the first row): Original normalized images. (the second row): Stripped skull images.

4.2. Parameter Setting

In the numerical implementation of RGK and other compared algorithms, we require to set constant parameters. In this study, three indispensable parameters including: the fuzzy exponent, the minimal error threshold, and the maximal number of iterations are set $q=2$, $\eta = 10^{-5}$ and 50 for RGK and other compared algorithms, respectively. In our proposed algorithm and those algorithms required, the window size used for Wiener filter is a window of size 3×3. Also, the used median filter for membership matrix filtering is a window 3×3. In MICO, degree of Legendre polynomials (P) is considered as $P=3$. In BCIFCMSNI based on reported parameters in [28], Sugeno's negation parameter value is set as $\beta = 1.7$, spatial regularization parameter value $\alpha = 1.5$, and neighbourhood size 3. In FCMPSO based on reported parameters in [22], the population size (n), inertia weight (ω), cognitive coefficient (c_1), and social coefficient (c_2) are set as $n=60$, $\omega=1$, and $c_1 = c_1 = 2$, respectively. Also, in FCMWOA [23], population size has been considered as $n=12$. Except the mentioned indispensable parameters and the number of cluster center, there is no other parameters for ARKFCM. In FRFCM, the structure element (SE) used for morphological reconstruction (MR) is a square of size 3×3. In RFCM based on reported parameters in [47], to control the decreasing rate of weighting matrix, the ξ parameter is considered $\xi=0.0008$. The standard deviation of image data is related to noise levels in RFCM. Therefore, the β parameter is set in virtue of the standard deviation of each channel.

4.2.3 Experimental Results on Brain Web Dataset

The segmentation performance is evaluated for simulated T1w and T2w brain MRI images with varying levels of noise (3% and 9%) and INU (20% and 40%) on slices 80 to 120. ***Figures 5-6*** illustrate the qualitative results obtained from a simulated MRI image (Brain Web) corrupted with 9% noise and 40% INU on axial slice 90 for T1w and T2w, respectively. ***Tables 1-3*** show the performance of different algorithms in the segmentation of WM, GM, and CSF on T1w images, measured in terms of average *DS*, *JS*, and *CS*, respectively. ***Tables 4-6*** show the performance of different algorithms in the segmentation of WM, GM, and CSF on T2w images, measured in terms of average *DS*, *JS*, and *CS*, respectively. Additionally, the average DS values for WM, GM, and CSF across slices 80 to 120 of the simulated Brain Web MRI image, with 9% noise and 40% INU, are depicted in ***Figure 7***. The following observations can be made from the obtained results:

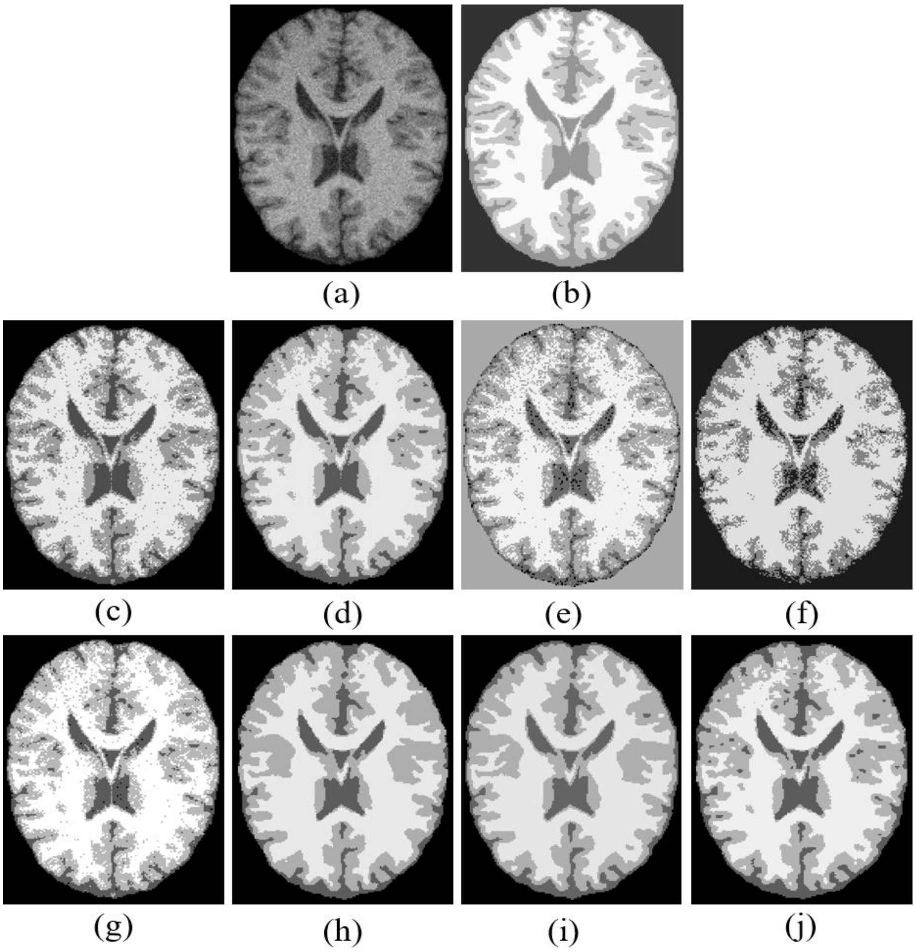

Figure 5. Qualitative segmentation performance on a simulated MRI image (Brain Web, T1w Image) with 9% noise and 40% INU. (a): Input image. (b): GT image. (c): MICO result. (d): ARKFCM result. (e): FCMPSO result. (f): FCMWOA result. (g): BCIFCMSNI result. (h): FRFCM result. (i): RFCM result. (j): Proposed RGK result.

Table 1. Comparison of the proposed RGK algorithm with other methods for WM segmentation on the Brain Web simulated dataset (T1w Images).

Criteria / Methods	*DS* (%) ↑				*JS* (%) ↑				*CS* (%) ↑			
	3% Noise		9% Noise		3% Noise		9% Noise		3% Noise		9% Noise	
	20% INU	40% INU	20% INU	40% INU	20% INU	40% INU	20% INU	40% INU	20% INU	40% INU	20% INU	40% INU
MICO	93.30	94.24	84.06	84.55	87.86	89.61	72.76	73.50	95.20	**97.15**	77.34	78.26
ARKFCM	94.96	92.91	93.11	90.63	91.90	86.88	87.19	82.97	98.57	93.55	94.27	89.80
FCMPSO	79.62	84.80	62.97	71.14	72.48	77.81	51.15	59.54	90.96	91.34	73.11	75.79
FCMWOA	91.76	88.65	80.35	82.20	85.51	81.55	69.31	70.88	92.52	87.27	76.92	77.76
BCIFCMSNI	88.89	84.87	85.76	85.25	81.91	76.08	75.44	74.97	80.09	69.95	82.13	78.66
FRFCM	94.17	94.26	93.52	91.79	91.75	89.18	87.88	85.19	97.93	95.48	96.66	93.25
RFCM	94.36	93.19	93.79	92.17	90.63	87.29	88.84	85.83	97.26	94.14	97.05	93.41
RGK	**96.94**	**95.37**	**94.15**	**92.88**	**93.23**	**90.38**	**89.12**	**86.30**	**98.63**	**97.15**	**97.97**	**95.33**

Table 2. Comparison of the proposed RGK algorithm with other methods for GM segmentation on the Brain Web simulated dataset (T1w Images).

Criteria / Methods	*DS* (%) ↑				*JS* (%) ↑				*CS* (%) ↑			
	3% Noise		9% Noise		3% Noise		9% Noise		3% Noise		9% Noise	
	20% INU	40% INU	20% INU	40% INU	20% INU	40% INU	20% INU	40% INU	20% INU	40% INU	20% INU	40% INU
MICO	87.52	89.10	75.04	75.69	78.30	80.61	60.33	61.20	**97.60**	**97.36**	91.90	92.20
ARKFCM	84.38	78.00	77.57	74.35	75.05	66.57	65.63	61.22	97.00	95.19	95.69	94.21
FCMPSO	67.34	67.86	59.15	58.82	52.28	57.22	45.45	44.66	92.63	91.64	88.40	88.22
FCMWOA	78.84	76.73	67.94	68.44	68.44	65.35	53.36	53.65	95.67	93.54	91.58	91.77
BCIFCMSNI	68.95	66.74	69.81	67.96	61.00	58.92	55.58	55.00	89.79	84.78	93.94	91.18
FRFCM	89.51	88.22	86.81	85.21	81.09	78.98	76.74	74.12	94.86	93.75	94.70	93.11
RFCM	89.27	87.13	**88.25**	86.01	80.66	77.21	78.80	75.22	95.04	94.08	95.41	94.19
RGK	**91.23**	**89.66**	87.81	**86.72**	**82.26**	**80.68**	**79.32**	**76.31**	96.87	96.80	**97.01**	**96.17**

Table 3. Comparison of the proposed RGK algorithm with other methods for CSF segmentation on the Brain Web simulated dataset (T1w Images).

Criteria / Methods	*DS* (%) ↑				*JS* (%) ↑				*CS* (%) ↑			
	3% Noise		9% Noise		3% Noise		9% Noise		3% Noise		9% Noise	
	20% INU	40% INU	20% INU	40% INU	20% INU	40% INU	20% INU	40% INU	20% INU	40% INU	20% INU	40% INU
MICO	**87.44**	**88.44**	82.70	83.37	**77.89**	**79.44**	70.70	71.67	**97.63**	**98.35**	**95.13**	95.07
ARKFCM	67.08	64.95	63.10	65.98	56.76	53.84	52.12	53.59	93.07	91.24	90.41	90.50
FCMPSO	72.41	80.39	65.03	65.66	62.27	71.56	51.22	52.37	92.62	94.78	88.33	88.94
FCMWOA	75.57	74.22	67.34	68.01	62.76	61.36	52.62	52.80	92.46	91.45	89.35	89.80
BCIFCMSNI	57.04	47.29	52.09	64.26	49.83	51.52	44.07	58.89	73.80	59.06	74.64	76.33
FRFCM	82.52	83.69	82.15	82.13	70.43	72.11	70.10	70.06	87.97	88.54	88.51	89.19
RFCM	83.73	83.62	83.80	83.08	72.07	71.92	**76.26**	71.18	89.00	89.52	89.98	91.02
RGK	85.59	84.66	**84.53**	**84.63**	74.61	74.72	73.91	**73.17**	94.52	94.40	**95.13**	**95.15**

Table 4. Comparison of the proposed RGK algorithm with other methods for WM segmentation on the Brain Web simulated dataset (T2w Images).

Criteria / Methods	*DS* (%) ↑				*JS* (%) ↑				*CS* (%) ↑			
	3% Noise		9% Noise		3% Noise		9% Noise		3% Noise		9% Noise	
	20% INU	40% INU	20% INU	40% INU	20% INU	40% INU	20% INU	40% INU	20% INU	40% INU	20% INU	40% INU
MICO	87.37	85.63	71.58	72.83	77.82	76.50	56.02	57.50	84.92	86.20	72.24	72.19
ARKFCM	46.84	50.61	62.09	41.69	43.35	46.19	51.40	32.08	79.29	82.57	79.16	74.29
FCMPSO	67.18	73.62	58.46	62.56	54.97	60.63	43.67	47.87	64.39	61.15	65.83	67.65
FCMWOA	54.11	46.92	50.26	57.78	45.18	38.68	36.17	42.70	51.30	43.12	63.32	67.62
BCIFCMSNI	30.98	40.05	52.14	53.10	28.26	36.25	41.07	41.62	32.11	41.32	56.07	57.72
FRFCM	89.68	87.82	83.83	82.82	81.54	78.58	72.40	70.95	92.47	87.33	78.66	74.94
RFCM	92.05	91.03	46.85	44.60	85.34	83.59	40.27	38.20	83.97	82.91	43.53	42.03
RGK	**93.63**	**92.44**	**88.30**	**87.91**	**88.11**	**86.02**	**79.12**	**78.50**	**97.65**	**96.27**	**88.62**	**87.71**

Table 5. Comparison of the proposed RGK algorithm with other methods for GM segmentation on the Brain Web simulated dataset (T2w Images).

Criteria / Methods	*DS* (%) ↑				*JS* (%) ↑				*CS* (%) ↑			
	3% Noise		9% Noise		3% Noise		9% Noise		3% Noise		9% Noise	
	20% INU	40% INU	20% INU	40% INU	20% INU	40% INU	20% INU	40% INU	20% INU	40% INU	20% INU	40% INU
MICO	78.33	78.27	64.40	64.72	64.59	64.61	47.64	47.94	95.14	95.51	86.29	86.99
ARKFCM	52.11	53.83	63.30	47.79	43.09	44.10	48.45	34.54	84.60	85.54	90.99	85.67
FCMPSO	47.51	43.62	46.26	52.55	36.63	33.85	32.37	37.56	84.70	82.61	84.72	86.66
FCMWOA	59.13	53.45	45.71	59.10	46.34	40.42	32.80	43.06	83.00	82.29	77.24	83.62
BCIFCMSNI	68.52	72.03	65.56	65.99	53.21	57.55	49.04	49.48	84.19	86.73	87.01	85.88
FRFCM	78.31	74.57	66.89	63.70	64.94	60.36	50.72	47.60	94.07	93.27	91.44	90.10
RFCM	64.23	65.47	30.06	31.91	47.51	48.80	18.33	19.66	92.69	92.95	81.76	83.26
RGK	**86.91**	**85.33**	**80.49**	**79.83**	**77.07**	**74.68**	**67.39**	**66.51**	**97.66**	**97.54**	**95.12**	**94.94**

Table 6. Comparison of the proposed RGK algorithm with other methods for CSF segmentation on the Brain Web simulated dataset (T2w Images).

Criteria / Methods	*DS* (%) ↑				*JS* (%) ↑				*CS* (%) ↑			
	3% Noise		9% Noise		3% Noise		9% Noise		3% Noise		9% Noise	
	20% INU	40% INU	20% INU	40% INU	20% INU	40% INU	20% INU	40% INU	20% INU	40% INU	20% INU	40% INU
MICO	86.49	87.31	83.39	83.81	77.85	79.15	71.77	72.35	95.26	98.12	94.14	94.73
ARKFCM	74.08	74.79	79.20	74.10	60.23	61.26	65.97	59.98	85.31	85.58	92.46	87.03
FCMPSO	64.54	69.16	64.86	55.02	54.51	58.50	54.50	44.45	90.63	90.76	90.31	87.51
FCMWOA	82.58	80.86	66.89	80.18	72.47	70.76	56.05	68.51	93.26	91.35	79.69	92.62
BCIFCMSNI	88.05	**90.91**	85.66	86.29	**80.14**	**83.54**	75.57	74.49	95.31	**98.79**	**96.66**	96.11
FRFCM	77.84	78.39	78.02	76.67	64.14	64.93	64.31	62.70	78.58	79.65	79.00	76.83
RFCM	47.11	48.01	39.60	41.35	31.13	31.99	24.87	26.29	72.93	67.32	59.51	60.33
RGK	**88.35**	88.08	**85.81**	**86.62**	78.66	77.76	**75.74**	**75.47**	**95.47**	96.23	94.72	**96.45**

(1) Based on ***Table 1 and Table 4***, the proposed RGK algorithm demonstrates the best performance for the segmentation of white matter (WM) on T1w and T2w images compared to other algorithms. The *CS* criterion indicates that the MICO algorithm lacks appropriate efficiency in recognizing the boundaries of WM under 9% noise and INU levels of 20% and 40% on T1w images. This algorithm has not an appropriate performance in T2w images. The ARKFCM algorithm performs well for WM segmentation; however, ***Figure 7*** illustrates that this algorithm is not suitable for slices numbered 99–104. Population-based approaches, such as FCMPSO and FCMWOA, show suitable performance under 9% noise and high levels of INU (20% and 40%). As shown in ***Figure 5(e)***, FCMPSO frequently mislabels the background class as the gray matter (GM) class. ***Figure 7*** indicates that FCMPSO is not appropriate for slices numbered 90–109, whereas FCMWOA performs better than FCMPSO for these slices. Furthermore, FCMWOA requires fewer fine-tuning parameters than FCMPSO, which makes PSO an unsuitable candidate for optimizing the FCM algorithm. Based on ***Tables 4-6***, population-based approaches have the worst performance in segmentation of MRI tissues on T2w images. BCIFCMSNI fails to correct the bias field for slices numbered 109–120. Additionally, based on the obtained *JS* criterion in ***Table 1***, this algorithm is unable to effectively segment WM. Under varying conditions of noise (3% and 9%) and INU (20% and 40%), three algorithms—FRFCM, RFCM, and RGK—exhibit

appropriate efficiency for WM segmentation. Based on ***Table 4***, the value of evaluation criteria decreases in WM segmentation on T2w images. Also, there is a difference of approximately 10% between proposed RGK algorithm and FRFCM in all parameters. These results the generalizability of the proposed algorithm to T2w MRI images. The use of the WFWT approach instead of morphological reconstruction (MR) has contributed to the RGK algorithm being more robust than both FRFCM and RFCM. According to ***Table 1***, the *CS* criterion demonstrates that RGK preserves edges well, resulting in proper contour matching in WM segmentation. Moreover, ***Figure 7*** illustrates that the proposed RGK algorithm performs effectively across all slices.

(2) As demonstrated in ***Table 2*** and ***Table5***, the proposed RGK algorithm is effective for gray matter (GM) segmentation under various noise and INU levels on T1w and T2w images, showcasing the best performance compared to other algorithms based on the *JS* criterion. Notably, the RGK algorithm is both robust and accurate for GM segmentation. In contrast, the MICO algorithm exhibits poor performance for GM segmentation according to the *DS* and *JS* criteria, making it less robust to noise and varying INU levels. As illustrated in ***Figure 6(c)***, this algorithm frequently mislabels the WM class as the GM class and has not a proper performance in segmentation of brain tissues on T2w images. However, based on the *CS* criterion, MICO performs well under 3% noise and high INU levels, indicating that it can identify GM boundaries with greater detail. Despite this, MICO struggles with high noise levels (9%) and does not segment GM effectively, whereas the RGK algorithm remains robust even with 9% noise and high INU levels (20% and 40%) on both T1w and T2w images. RGK achieves an average *CS* value of 97% (for T1w images) and 95% (for T2w images) for 9% noise and 20% INU, demonstrating its superior performance in GM segmentation. It also exhibits the highest *CS* value under 9% noise and 40% INU. The *CS* criterion results in ***Table 2*** further indicate that RGK effectively preserves edges with more detail. Due to incorrect labeling of the background class as the GM class, FCMPSO shows the worst performance for GM segmentation across different noise and INU conditions. Although FCMWOA demonstrates better efficiency than FCMPSO under low noise conditions, it is not robust under high noise levels. Based on ***Figure 6(e and f)***, in segmentation of brain tissues based on T2w images, FCMPSO algorithm frequently mislabels the WM class as the GM class and FCMWOA mislabels the GM class as the WM class. As shown in ***Figure 7***, BCIFCMSNI performs well on slices 80–85 and 92–102 but is not a suitable candidate for other slices, which adversely affects its performance for GM segmentation. Also, this algorithm has not a suitable performance in GM tissue segmentation on T2w images. Overall, RGK outperforms its peers in terms of the *DS* criterion. As illustrated in ***Figure 5*** and ***Figure 6***, the proposed RGK algorithm segments GM pixels with greater detail on both T1w and T2w images.

(3) The CSF region consists of compact and small clusters; thus, FCM-based approaches do not perform well using Euclidean distance. As illustrated in ***Figure 5(j)***, both FRFCM and RFCM incorrectly label CSF and GM pixels. ***Table 3*** shows that FCM-based methods are not suitable for CSF segmentation, particularly when the clusters in the data differ in size and shape. This underscores the effectiveness of the proposed RGK algorithm, which is adept at detecting ellipsoidal cloud clusters with varying sizes and orientations. MICO, being a contour-based approach, also demonstrates suitability for the segmentation of compact and small clusters. ***Table 3*** reveals that MICO and RGK achieve similar results in CSF segmentation across different noise and INU conditions. However, as indicated in ***Figure 7***, MICO exhibits

suboptimal performance for slices 100-110, while the proposed RGK algorithm remains stable across all slices. The obtained experimental results on both T1w and T2w images illustrate the generalizability of the proposed RGK algorithm for CSF region segmentation.

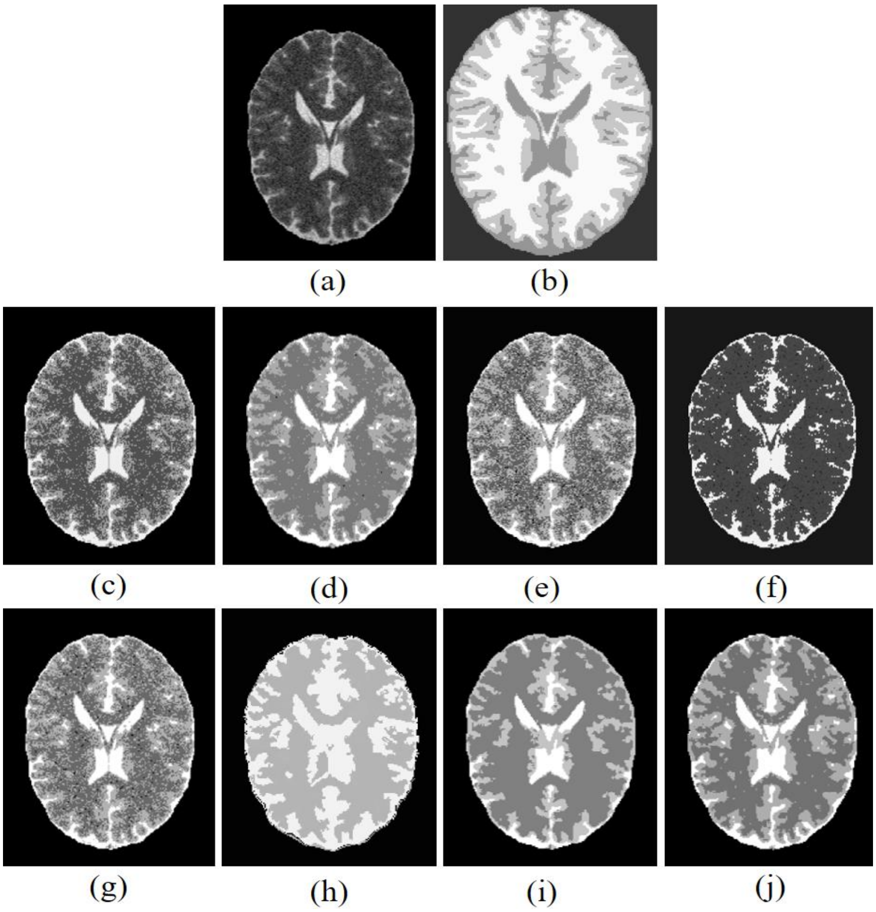

Figure 6. Qualitative segmentation performance on a simulated MRI image (Brain Web, T2-weighted Image) with 9% noise and 40% INU. (a): Input image. (b): GT image. (c): MICO result. (d): ARKFCM result. (e): FCMPSO result. (f): FCMWOA result. (g): BCIFCMSNI result. (h): FRFCM result. (i): RFCM result. (j): Proposed RGK result.

The average running times for the various algorithms are presented in ***Table 7***. These results indicate that population-based algorithms, such as FCMPSO and FCMWOA, are time-consuming. Contour-based methods like MICO are also more time-intensive due to their reliance on edge-stopping functions that depend on the image gradient. In contrast, FRFCM and RFCM exhibit the lowest execution times among the algorithms assessed. However, the main drawback of these algorithms is their inefficacy when clusters in the data are not of the same size and shape.

Table 7. Comparison of average execution times of different algorithms on the Brain Web dataset (in seconds, 9% noise and 40% INU).

Brain Image Size	MICO	ARKFCM	FCMPSO	FCMWOA	BCIFCMSNI	FRFCM	RFCM	RGK
181×217	4.17	1.87	4.15	3.05	2.85	**0.05**	**0.62**	2.15

To further compare and analyze the proposed method, it is beneficial to explore deep learning approaches as well. In recent years, these methods have demonstrated their unique capabilities in tasks such as medical image segmentation [56]. The foundation of most of these methods is based on convolutional neural networks (CNNs). U-Net networks, for instance, are a highly successful example of CNNs in medical image segmentation. In this study, we utilize a new, well-established model known as SynthSeg as a representative of deep learning-based methods for comparison and performance evaluation. SynthSeg is a convolutional neural network designed for brain MRI segmentation across different contrasts and resolutions without requiring retraining. Traditional CNN models often struggle with generalization due to variations in factors such as resolution and contrast. To address this challenge, SynthSeg employs a domain randomization strategy during training, where synthetic data is generated based on segmented models. By fully randomizing the contrast and resolution of these synthetic images, SynthSeg achieves a high level of robustness, allowing it to effectively segment real scans from diverse domains. This method enables the analysis of large and heterogeneous clinical datasets. SynthSeg requires only segmentation labels and does not rely on real images. This feature allows the model to learn from labels obtained through automated methods across different populations, making it resistant to various morphological variations. Evaluations on 5,000 scans across six modalities and ten different resolutions have shown that SynthSeg outperforms traditional supervised CNNs, advanced domain adaptation methods, and Bayesian segmentation approaches [57]. Furthermore, SynthSeg has also been successfully applied to cardiac MRI and CT scan processing, demonstrating its high adaptability. The enhanced version of this model offers more precise segmentation, cortical parcellation, intracranial volume estimation, and automatic error detection. This version has been optimized for processing heterogeneous clinical data and has demonstrated successful performance in large-scale studies, such as aging trend analysis on 14,000 scans [58]. The performance of proposed RGK algorithm has been compared with SynthSeg approach in segmentation of brain tissues on the Brain Web simulated dataset (T1w and T2w Images) in ***Table 8***. The experimental results indicate the performance of proposed algorithm is close to SynthSeg method and in some cases even better than the SynthSeg method.

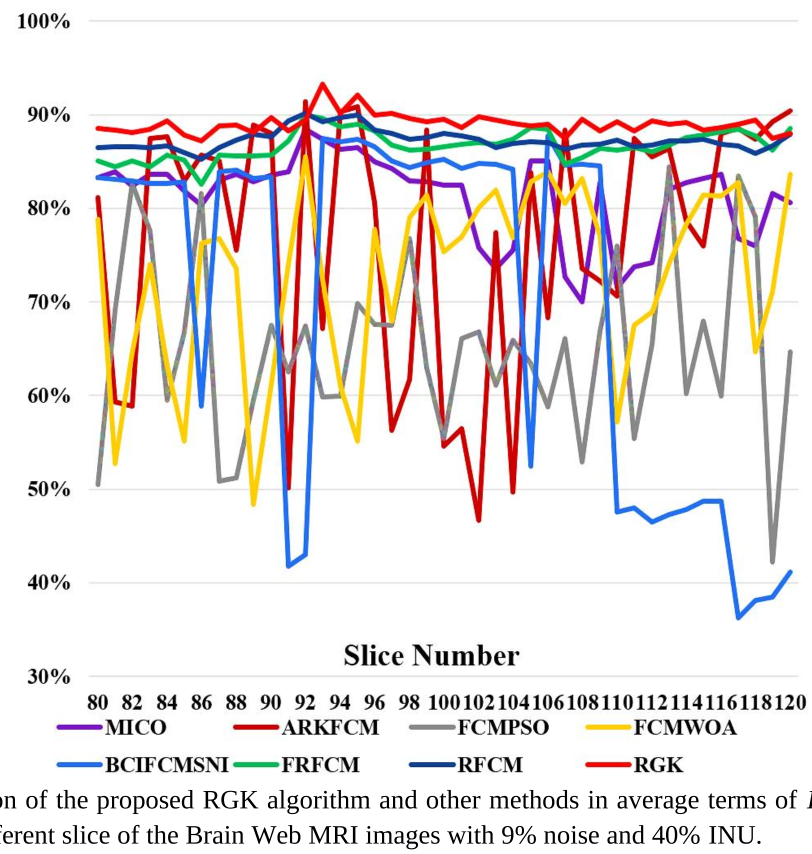

Figure 7. Comparison of the proposed RGK algorithm and other methods in average terms of *DS* criterion for WM, GM, and CSF on different slice of the Brain Web MRI images with 9% noise and 40% INU.

Table 8. Comparison of the proposed RGK algorithm with SynthSeg method for segmentation of brain tissues on the Brain Web simulated dataset (T1w and T2w Images).

White Matter												
Criteria / Methods	*DS* (%) ↑ (T1w)				*JS* (%) ↑ (T1w)				*CS* (%) ↑ (T1w)			
	3% Noise		9% Noise		3% Noise		9% Noise		3% Noise		9% Noise	
	20% INU	40% INU	20% INU	40% INU	20% INU	40% INU	20% INU	40% INU	20% INU	40% INU	20% INU	40% INU
SynthSeg	94.71	94.73	93.33	**93.45**	90.04	90.08	87.59	**87.80**	97.74	**97.73**	96.53	**96.77**
RGK	**96.94**	**95.37**	**94.15**	92.88	**93.23**	**90.38**	**89.12**	86.30	**98.63**	97.15	**97.97**	95.33
Criteria / Methods	*DS* (%) ↑ (T2w)				*JS* (%) ↑ (T2w)				*CS* (%) ↑ (T2w)			
	3% Noise		9% Noise		3% Noise		9% Noise		3% Noise		9% Noise	
	20% INU	40% INU	20% INU	40% INU	20% INU	40% INU	20% INU	40% INU	20% INU	40% INU	20% INU	40% INU
SynthSeg	92.93	**92.95**	**88.47**	**88.87**	86.91	**86.93**	**79.45**	**80.09**	96.38	**96.41**	**88.67**	**89.57**
RGK	**93.63**	92.44	88.30	87.91	**88.11**	86.02	79.12	78.50	**97.65**	96.27	88.62	87.71
Grey Matter												
Criteria / Methods	*DS* (%) ↑ (T1w)				*JS* (%) ↑ (T1w)				*CS* (%) ↑ (T1w)			
	3% Noise		9% Noise		3% Noise		9% Noise		3% Noise		9% Noise	
	20% INU	40% INU	20% INU	40% INU	20% INU	40% INU	20% INU	40% INU	20% INU	40% INU	20% INU	40% INU
SynthSeg	88.40	88.39	86.90	**87.10**	79.27	79.24	76.87	**77.20**	96.36	96.35	95.58	95.68
RGK	**91.23**	**89.66**	**87.81**	86.72	**82.26**	**80.68**	**79.32**	76.31	**96.87**	**96.80**	**97.01**	**96.17**
Criteria / Methods	*DS* (%) ↑ (T2w)				*JS* (%) ↑ (T2w)				*CS* (%) ↑ (T2w)			
	3% Noise		9% Noise		3% Noise		9% Noise		3% Noise		9% Noise	
	20% INU	40% INU	20% INU	40% INU	20% INU	40% INU	20% INU	40% INU	20% INU	40% INU	20% INU	40% INU
SynthSeg	**87.59**	**87.58**	**81.33**	**81.97**	**77.98**	**77.95**	**68.59**	**69.52**	96.00	96.01	92.19	92.61
RGK	86.91	85.33	80.49	79.83	77.07	74.68	67.39	66.51	**97.66**	**97.54**	**95.12**	**94.94**
Cerebrospinal Fluid												
Criteria / Methods	*DS* (%) ↑ (T1w)				*JS* (%) ↑ (T1w)				*CS* (%) ↑ (T1w)			
	3% Noise		9% Noise		3% Noise		9% Noise		3% Noise		9% Noise	
	20% INU	40% INU	20% INU	40% INU	20% INU	40% INU	20% INU	40% INU	20% INU	40% INU	20% INU	40% INU
SynthSeg	79.04	78.95	79.68	79.72	65.39	65.28	66.29	66.33	**95.02**	**94.98**	94.72	94.72
RGK	**85.59**	**84.66**	**84.53**	**84.63**	**74.61**	**74.72**	**73.91**	**73.17**	94.52	94.40	**95.13**	**95.15**
Criteria / Methods	*DS* (%) ↑ (T2w)				*JS* (%) ↑ (T2w)				*CS* (%) ↑ (T2w)			
	3% Noise		9% Noise		3% Noise		9% Noise		3% Noise		9% Noise	
	20% INU	40% INU	20% INU	40% INU	20% INU	40% INU	20% INU	40% INU	20% INU	40% INU	20% INU	40% INU
SynthSeg	83.63	83.60	82.12	82.62	71.91	71.88	69.73	70.47	**95.99**	95.94	**95.59**	95.86
RGK	**88.35**	**88.08**	**85.81**	**86.62**	**78.66**	**77.76**	**75.74**	**75.47**	95.47	**96.23**	94.72	**96.45**

4.4. Experimental Results on GMICT Dataset

(1) In this section, we evaluate the segmentation performance of GMICT MRI T1w brain images. ***Figure 8*** presents the qualitative results obtained from a GMICT image. ***Table 9*** summarizes the performance of various algorithms in segmenting WM, GM, and CSF based on average values of the *DS*, *JS*, and *CS* criteria. Additionally, ***Figure 9*** depicts a boxplot illustrating the average *DS* criterion values for WM, GM, and CSF. The following observations can be drawn from the results obtained: ***Table 9*** manifests that the proposed RGK algorithm has the highest

values in terms of *DS*, *JS*, and *CS* criteria for segmentation of tissues compared to other algorithms.

(2) Population-based approaches (FCMPSO and FCMWOA) have the worst performance. Based on ***Figure 8(i)***, in FCMPSO, the WM class is incorrectly labelled as GM class, usually. Also, as shown in ***Figure 8(f)***, in FCMWOA, the CSF class is incorrectly labelled as back-ground class, usually.

(3) As shown in ***Figure 8(g)***, BCIFCMSNI doesn't efficiently work in some GMICT dataset and identify GM pixels as WM pixels, incorrectly. This algorithm has the lowest value in term of *CS* criterion. It reveals that this algorithm cannot recognize the boundary with more details.

(4) FRFCM, RFCM, and RGK algorithms have an appropriate performance for segmentation of tissues on GMICT dataset. CSF plays a vital role in clearing metabolic waste from the human brain. Therefore, accurate segmentation of CSF is a valuable task. CSF is usually considered as a compact and small cluster. ***Table 9*** illustrates that FCM-based methods are not a proper tool for this purpose. RGK by using the Mahalanobis distance instead of Euclidean distance is a suitable candidate for clustering the compact data.

(5) ***Figure 9*** depicts that the proposed RGK algorithm has higher segmentation accuracy for tissues compared to other algorithms. It is valuable that the RGK has the lowest standard deviation value.

(6) The average running times for different algorithms has been demonstrated in ***Table 10***. These results reveal that the population-based algorithms (FCMPSO and FCMWOA) are time-consuming. Contour-based methods such as MICO take more time. FRFCM and RGK algorithms have the lowest execution times compared to other algorithms.

Table 9. Comparison of the proposed RGK algorithm with other methods for MRI image segmentation on GMICT dataset.

Criteria / Methods	*DS* (%) ↑			*JS* (%) ↑			*CS* (%) ↑		
	WM	GM	CSF	WM	GM	CSF	WM	GM	CSF
MICO	80.41	62.51	76.22	68.69	46.16	62.63	75.71	89.69	91.62
ARKFCM	83.31	71.43	70.68	75.72	60.95	59.11	81.33	91.77	91.41
FCMPSO	84.14	67.89	62.74	75.27	56.01	51.15	79.74	89.05	84.34
FCMWOA	72.63	35.23	39.26	61.01	37.13	38.37	49.32	69.71	65.99
BCIFCMSNI	78.23	72.89	76.81	74.69	61.13	60.12	70.78	81.13	70.15
FRFCM	88.20	81.46	81.63	81.39	70.34	70.49	86.63	90.66	91.12
RFCM	88.10	80.39	79.09	81.21	68.58	66.35	86.15	90.22	88.25
RGK	**90.24**	**82.16**	**84.89**	**82.70**	**71.40**	**74.62**	**88.95**	**92.77**	**94.18**

Table 10. Comparison of average execution times of different algorithms on GMICT dataset (in seconds).

Brain Image Size	MICO	ARKFCM	FCMPSO	FCMWOA	BCIFCMSNI	FRFCM	RFCM	RGK
256×256	5.10	2.7	7.1	5.2	3.4	**0.03**	1.33	**0.8**

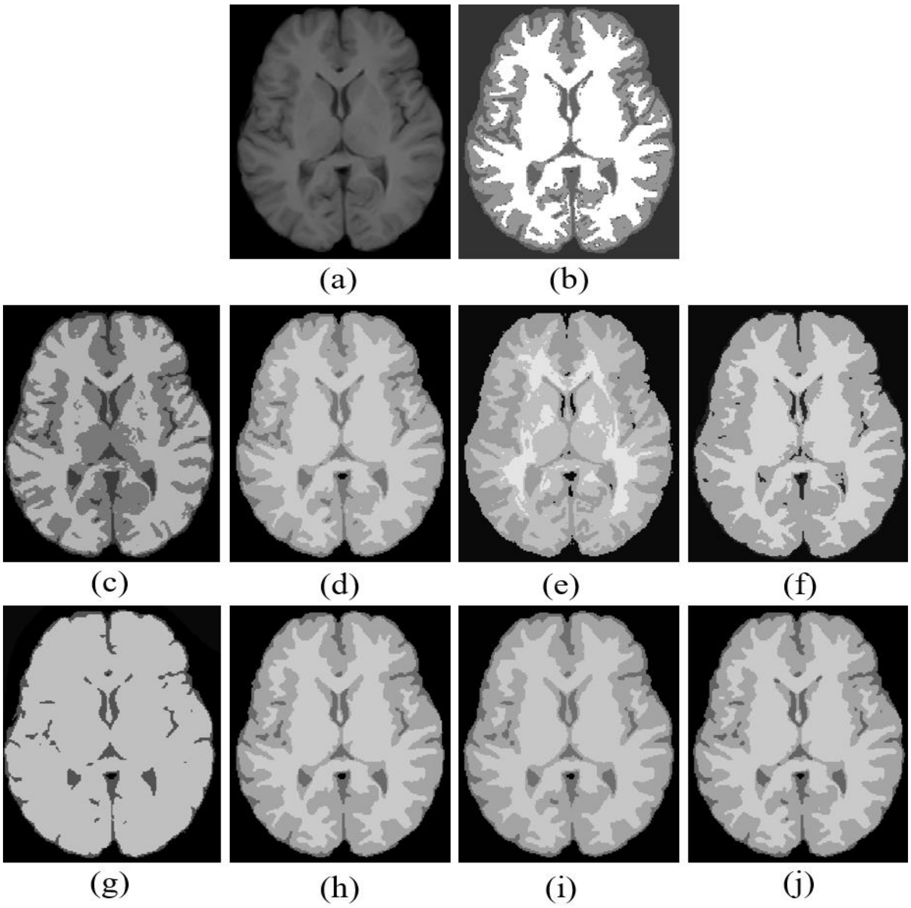

Figure 8. Qualitative segmentation performance on GMICT image. (a): Input image. (b): GT image. (c): MICO result. (d): ARKFCM result. i: FCMPSO result. (f): FCMWOA result. (g): BCIFCMSNI result. (h): FRFCM result. (i): RFCM result. (j): Proposed RGK result.

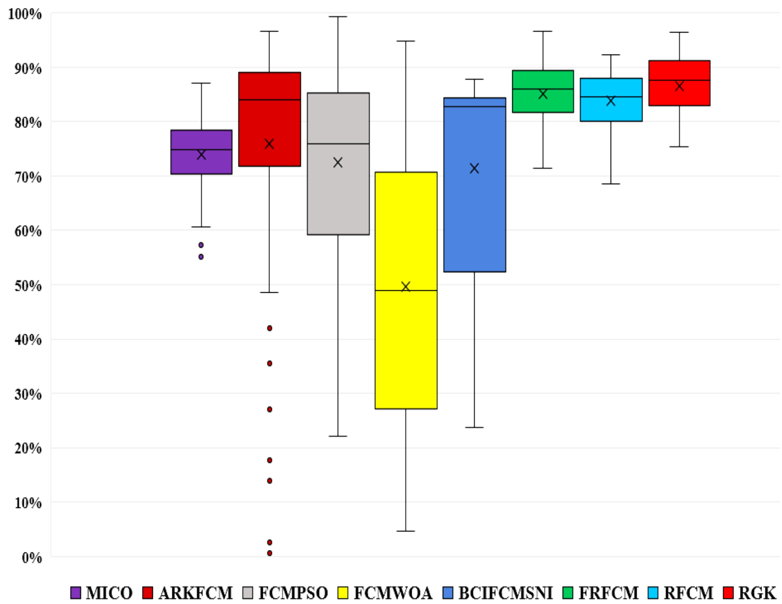

Figure 9. Boxplot for comparison of the proposed RGK algorithm and other methods in average terms of *DS* criterion for WM, GM, and CSF on GMICT dataset.

5. Conclusion and Future Works

FCM-based methods rely on the Euclidean distance for clustering, which fails to account for variations in the distances of data points within similar and compact clusters. This limitation is especially problematic for cerebrospinal fluid (CSF), which plays a crucial role in clearing metabolic waste from the brain and often appears as a small, compact cluster. The use of the Euclidean distance can cause this cluster to be misclassified. Additionally, noise and INU significantly impact the clustering process, increasing the number of iterations required for FCM and GK algorithms when segmenting noisy images. Under these conditions, obtaining a clear image histogram for fast segmentation becomes challenging. To address the mentioned problems, this study proposed a robust Gustafson-Kessel (RGK) algorithm for segmenting brain tissues based on T1-weighted MRI images. The RGK algorithm avoids the need to compute distances between pixels within local spatial neighborhoods. At first, a Wiener filter combined with WFWT was applied to improve image quality under different noise and INU levels while preserving object edges. In the second step, the image histogram was used for fast segmentation, followed by clustering using the Mahalanobis distance instead of the Euclidean distance. In the final step, RGK incorporated membership matrix filtering to exploit local spatial constraints. The proposed algorithm is efficiently fast and does not require parameter tuning. It was evaluated on two datasets: the BrainWeb simulated dataset and MRI scans from 10 healthy individuals at the Golghasht Medical Imaging Center in Tabriz (GMICT), Iran. For the GMICT dataset, the remnants of brain extraction were used to obtain consistent values across slices and scans over time. Experimental results showed that the RGK algorithm is accurate for segmenting tissues and robust to various noise and INU levels, delivering reliable performance across all slices. The proposed algorithm can be applied on other medical images such as C.T, X-ray and ultrasound images. In medical image analysis such as C.T, the number of cluster centers is experimentally set. Therefore, in future work, it would be beneficial to develop a GK algorithm that can automatically determine the number of clusters. Additionally, incorporating a bias field term into the RGK cost function could further improve the algorithm's performance.

References

[1] Kouhi, A et al, "Robust FCM clustering algorithm with combined spatial constraint and membership matrix local information for brain MRI segmentation," Expert Systems with Applications, vol. 146, pp. 113159, 2020.

[2] Emam, M. M et al, "A modified reptile search algorithm for global optimization and image segmentation: Case study brain MRI images," Computers in biology and medicine, vol. 152, pp. 106404, 2023.

[3] Bandyopadhyay, R et al, "Segmentation of brain MRI using an altruistic Harris Hawks' Optimization algorithm," *Knowledge-Based Systems*, vol. 232, pp. 107468, 2021.

[4] Li, C et al, "Multiplicative intrinsic component optimization (MICO) for MRI bias field estimation and tissue segmentation," *Magnetic resonance imaging*, vol. 32, no. 7, pp. 913-923, 2014.

[5] Hassan, M et al, "Robust spatial fuzzy GMM based MRI segmentation and carotid artery plaque detection in ultrasound images," *Computer methods and programs in biomedicine*, vol. 175, pp. 179-192, 2019.

[6] Singh, C et al, "An Intuitionistic Fuzzy C-Means and Local Information-Based DCT Filtering for Fast Brain MRI Segmentation," *Journal of Imaging Informatics in Medicine*, pp. 1-24., 2024.

[7] Jafrasteh, B et al, "Enhanced Spatial Fuzzy C-Means Algorithm for Brain Tissue Segmentation in T1 Images," *Neuroinformatics*, pp. 1-14, 2024.

[8] Singh, C et al, "A novel approach for brain MRI segmentation and image restoration under intensity inhomogeneity and noisy conditions," *Biomedical Signal Processing and Control*, vol. 87, pp. 105348, 2024.

[9] Natarajan, S et al, "Minimally parametrized segmentation framework with dual metaheuristic optimisation algorithms and FCM for detection of anomalies in MR brain images," *Biomedical Signal Processing and Control*, vol. 78, pp. 103866, 2022.

[10] Houssein, E. H et al, "Accurate multilevel thresholding image segmentation via oppositional Snake Optimization algorithm: Real cases with liver disease," *Computers in Biology and Medicine*, vol. 169, pp. 107922, 2024.
[11] H. Essam et al, "An efficient multilevel thresholding segmentation method for thermography breast cancer imaging based on improved chimp optimization algorithm," *Expert Systems with Applications*, vol. 185, pp. 115651, 2021.
[12] M. Guoyuan and X. Yue, "An improved whale optimization algorithm based on multilevel threshold image segmentation using the Otsu method," *Engineering Applications of Artificial Intelligence*, vol. 113, pp. 104960, 2022.
[13] Lang, T and Sauer, T, "Feature-Adaptive Interactive Thresholding of Large 3D Volumes. a*rXiv preprint arXiv:2210.06961*, 2022.
[14] D. Bin et al, "An active contour model based on shadow image and reflection edge for image segmentation," *Expert Systems with Applications*, vol. 238, pp. 122330, 2024.
[15] C. Yiyang et al, "An active contour model for image segmentation using morphology and nonlinear Poisson's equation," *Optik*, vol. 287, pp. 170997, 2023.
[16] Zia, H et al, "Active Contour Model for Image Segmentation," *Asia Conference on Advanced Robotics, Automation, and Control Engineering (ARACE)*, pp. 13-17, 2022.
[17] Adhikari, S. K et al, "Conditional spatial fuzzy C-means clustering algorithm for segmentation of MRI images," *Applied soft computing*, vol. 34, pp. 758-769, 2015.
[18] Elazab, A et al, "Segmentation of brain tissues from magnetic resonance images using adaptively regularized kernel-based fuzzy C-means clustering," *Computational and mathematical methods in medicine*, vol. 2015, no. 1, pp. 485495, 2015.
[19] Bakhshali, M. A, "Segmentation and enhancement of brain MR images using fuzzy clustering based on information theory," *Soft Computing*, vol. 21, pp. 6633-6640., 2017.
[20] Moeskops, P et al, "Automatic segmentation of MR brain images with a convolutional neural network," *IEEE transactions on medical imaging*, vol. 35, no. 5, pp. 1252-1261, 2016.
[21] Ghosh, P et al, "Chaotic firefly algorithm-based fuzzy C-means algorithm for segmentation of brain tissues in magnetic resonance images," *Journal of Visual Communication and Image Representation*, vol. 54, pp. 63-79., 2018.
[22] Verma, H et al, "A population-based hybrid FCM-PSO algorithm for clustering analysis and segmentation of brain image," *Expert systems with applications*, vol. 167, pp. 114121, 2021.
[23] Tongbram, S and et al, "A novel image segmentation approach using fcm and whale optimization algorithm," *Journal of ambient intelligence and humanized computing*, pp. 1-15., 2021.
[24] Chighoub, F and Saouli, R, "Fully integrated spatial information to improve FCM algorithm for brain MRI Image segmentation," *Automatic Control and Computer Sciences*, vol. 56, no. 1, pp. 67-82., 2022.
[25] Kumar, D et al, "Kernel picture fuzzy clustering with spatial neighborhood information for MRI image segmentation," *Soft Computing*, vol. 26, no. 22, pp. 12717-12740, 2022.
[26] Khaled, A et al, "Learning to detect boundary information for brain image segmentation," *BMC bioinformatics*, vol. 23, no. 1, pp. 332, 2022.
[27] Khatri, I et al, "A noise robust kernel fuzzy clustering based on picture fuzzy sets and KL divergence measure for MRI image segmentation," *Applied Intelligence*, vol. 53, no. 13, pp. 16487-16518, 2023.
[28] Kumar, D et al, "Bias-corrected intuitionistic fuzzy c-means with spatial neighborhood information approach for human brain MRI image segmentation," *IEEE Transactions on Fuzzy Systems*, vol. 30, no. 3, pp. 687-700, 2020.
[29] Kollem, S et al, "Brain tumor MRI image segmentation using an optimized multi-kernel FCM method with a pre-processing stage," *Multimedia Tools and Applications*, vol. 82, no. 14, pp. 20741-20770, 2023.
[30] Solanki, R and Kumar, D, "Probabilistic intuitionistic fuzzy c-means algorithm with spatial constraint for human brain MRI segmentation," *Multimedia Tools and Applications*, vol. 82, no. 22, pp. 33663-33692, 2023.
[31] Alagarsamy, S and et al, "Automated brain tumor segmentation for MR brain images using artificial bee colony combined with interval type-II fuzzy technique," *IEEE Transactions on Industrial Informatics*, vol. 19, no. 11, pp. 11150-11159, 2023.
[32] Kalti, K and Touil, A, "A Robust Contextual Fuzzy C-Means Clustering Algorithm for Noisy Image Segmentation," *Journal of Classification*, vol. 40, no. 3, pp. 488-512, 2023.
[33] Mohammadi, S et al, "Automated segmentation of meningioma from contrast-enhanced T1-weighted MRI images in a case series using a marker-controlled watershed segmentation and fuzzy C-means

clustering machine learning algorithm," *International Journal of Surgery Case Reports*, vol. 111, pp. 108818, 2023.
[34] Shekari, M and Rostamian, M, "Brain tumor segmentation from MRI using FCM clustering, morphological reconstruction, and active contour," *Multimedia Tools and Applications*, vol. 83, no. 14, pp. 42973-42998, 2024.
[35] Tian, Z and Wang, S, "A level set model with shape prior constraint for intervertebral disc MRI image segmentation," *Multimedia Tools and Applications*, pp. 1-29, 2024.
[36] Dunning, P. D and Kim, H. A, "Introducing the sequential linear programming level-set method for topology optimization," *Structural and Multidisciplinary Optimization*, vol. 51, pp. 631-643, 2015.
[37] Jafargholkhanloo, A. F. and Shamsi, M, "Cephalometry analysis of facial soft tissue based on two orthogonal views applicable for facial plastic surgeries," *Multimedia Tools and Applications*, vol. 82, no. 20, pp. 30643-30668, 2023.
[38] J. C. Bezdek et al, "FCM: The fuzzy c-means clustering algorithm," *Comput. Geosci*, vol. 10, no. 2-3, pp. 191-203, 1984.
[39] K. Raghu and J. Kim, "A note on the Gustafson-Kessel and adaptive fuzzy clustering algorithms," *IEEE Transactions on Fuzzy systems*, vol. 7, no. 4, pp. 453-461, 1999.
[40] D. Dejan and I. Škrjanc, "Recursive clustering based on a Gustafson–Kessel algorithm," *Evolving systems*, vol. 2, no. 1, pp. 15-24, 2011.
[41] B. R. P. J. Veen and U. Kaymak, "Improved covariance estimation for Gustafson-Kessel clustering," *IEEE International Conference on Fuzzy Systems*, vol. 2, 2002.
[42] G. Donald and W. C. Kessel, "Fuzzy clustering with a fuzzy covariance matrix," *IEEE conference on decision and control including the 17th symposium on adaptive processes*, 1979.
[43] S. László et al, "MR brain image segmentation using an enhanced fuzzy c-means algorithm," *Proceedings of the 25th annual international conference of the IEEE engineering in medicine and biology society*, vol. 1, 2003.
[44] L. Tao et al, "Significantly fast and robust fuzzy c-means clustering algorithm based on morphological reconstruction and membership filtering," *IEEE Transactions on Fuzzy Systems*, vol. 26, no. 5, pp. 3027-3041, 2018.
[45] Göreke, V, "A novel method based on Wiener filter for denoising Poisson noise from medical X-Ray images," *Biomedical Signal Processing and Control*, vol. 79, pp. 104031, 2023.
[46] Shreyamsha Kumar, B. K, "Image denoising based on non-local means filter and its method noise thresholding," *Signal, image and video processing*, vol. 7, pp. 1211-1227, 2013.
[47] W. Cong et al, "Residual-driven fuzzy C-means clustering for image segmentation," *IEEE/CAA Journal of Automatica Sinica*, vol. 8, no. 4, pp. 876-889, 2020.
[48] Jafargholkhanloo, A. F and Shamsi, M, "Quantitative analysis of facial soft tissue using weighted cascade regression model applicable for facial plastic surgery," *Signal Processing: Image Communication*, 121, 117086, 2024.
[49] https://brainweb.bic.mni.mcgill.ca/cgi/brainweb1
[50] M. Shah et al., "Evaluating intensity normalization on MRIs of human brain with multiple sclerosis," *Med. Image Anal*, vol. 15, no. 2, pp. 267–282, 2011.
[51] R. T. Shinohara et al., "Statistical normalization techniques for magnetic resonance imaging," *NeuroImage Clin*, vol. 6, pp. 9–19, 2014.
[52] Fortin, Jean-Philippe et al, "Harmonization of cortical thickness measurements across scanners and sites," *Neuroimage*, vol. 167, pp. 104-120, 2018.
[53] M. Jenkinson et al, "FSL," *Neuroimage*, vol. 62, no. 2, pp. 782–790, 2012.
[54] R. R. Edelman, J. R. Hesselink, M. B. Zlatkin, and J. V. Crues, Clinical magnetic resonance imaging, vol. 1, WB Saunders, 2006.
[55] C. Westbrook, C. K. Roth, and J. Talbot, MRI in Practice, 4th ed. Chichester, England: Wiley-Blackwell, 2011.
[56] R. Wang et al, "Medical image segmentation using deep learning: A survey," *IET Image Process*, vol. 16, no. 5, pp. 1243–1267, 2022.
[57] B. Billot et al, "SynthSeg: Segmentation of brain MRI scans of any contrast and resolution without retraining," *Med. Image Anal*, vol. 86, no. 102789, p. 102789, 2023.
[58] B. Billot et al, "Robust machine learning segmentation for large-scale analysis of heterogeneous clinical brain MRI datasets," Proc. Natl. Acad. Sci. U. S. A, vol. 120, no. 9, p. e2216399120, 2023.